AST325 Lab 4: Radio Telescopes and Pulsars

Shimona Das

Student Number: 1008964943

Group N

January 2025

Abstract

This lab investigates the performance of the Algonquin Radio Observatory's 46m radio telescope and the pulsar B0329+54 through calibration and analysis of archival data. Key properties of the telescope such as beamwidth, noise temperature, and aperture efficiency were measured then and compared to theoretical expectations. The measured Full Width at Half Maximum (FWHM) closely aligned with the theoretical diffraction limit at higher frequencies, with deviations at lower frequencies attributed to atmospheric effects and instrumental inefficiencies. Pulsar B0329+54 was also analysed using dispersion correction, pulse folding, and matched filtering techniques. The dispersion measure (DM) of was used to correct for frequency dependent time delays caused by the interstellar medium (ISM), resulting in vertically aligned pulses across all frequencies. The flux density near 675 MHz was calculated to be 1.75×10^{-23} W/m^2/Hz with an effective aperture of 1080.24 m^2 and a source temperature of 684.0 K. While the telescope performed near optimal resolution at higher frequencies, limitations such as radio frequency interference (RFI) and gain variability were noticed which suggest areas for improvement in future observations. This study demonstrates the capabilities of the ARO telescope in Canada and highlights the importance of advanced data reduction techniques in pulsar analysis.

1 Introduction

The detection and analysis of electromagnetic radiation across a range of wavelengths are essentially the foundation of modern astronomy. Radio astronomy, in particular, focuses on long-wavelength signals and uses instruments to observe celestial phenomena that would be otherwise invisible in other regions of the spectrum. Radio telescopes help in this endeavour by capturing faint radio signals from distant sources and enabling precise measurements.

In this experiment, archival data from the Algonquin Radio Observatory (ARO), which is Canada's largest single dish radio telescope, is used to explore key properties of the instrument and investigate the behaviour of pulsars, a class of rapidly rotating neutron stars that emit periodic bursts of electromagnetic radiation. The 46 meter aperture of the ARO dish allows for significant sensitivity enhancements which also allows the study of phenomena such as beamwidth, system noise temperature, and pulsar signal variability.

This lab in particular investigates the coupling of radio feeds with reflectors to understand how they ultimately influence system performance. The role of the feed's radiation pattern and the forward gain of the antenna is then examined in the context of system efficiency, particularly the challenges posed by illumination and spillover effects. Furthermore, principles such as the radiometer equation and the Rayleigh-Jeans approximation are applied to derive thermal equivalents for received signals, facilitating the calibration of system temperature and gain.

A specific focus of this lab involved analysis of pulsar B0329+54, a bright northern hemisphere pulsar. The dispersion of pulsar signals due to the interstellar medium (ISM) is also explored using the concept of dispersion measure, with subsequent de-dispersion to correct for frequency dependent time delays. Additionally, matched filtering and pulse folding techniques are applied to characterise the pulsar's emission profile, variability, and average pulse structure.

This report begins by detailing the experimental setup and methods used to analyse archival data from ARO. The next section discusses the calibration and characterization of the telescope's beamwidth and noise temperature. The following section presents a comprehensive analysis of pulsar B0329+54, focusing on data reduction, dispersion, and pulse variability. Finally, the results are contextualised within

the broader framework of radio astronomy, emphasizing the interplay between instrumental design and observational goals.

2   Data and Observation

Specification	Algonquin 46m Radio Telescope
Location	Algonquin Provincial Park, Ontario, Canada
Focal Ratio	f/0.4
Aperture Diameter	46 meters (150 feet)
Frequency Range	400-800 MHz
Surface Accuracy	1/5 of a centimeter
Latitude and Longitude	45.95°N, -78.07° W
Operational Wavelength Range	2 cm to 10.7 cm
Beamwidth calculation	Diffraction-limited FWHM
Efficiency	50-70%
Primary Use	Galactic and extragalactic radio source observation

Table 1: Properties of the Algonquin 46m Radio Telescope used to capture data for Cassiopeia A and Pulsar B0329+54

Property	Value
Telescope	Very Large Array (VLA)
Center (Coordinates)	RA: 23:21:13, Dec: 58:32:35
Distance	11,000 light-years
Angular Size	5 arcminutes
Physical Diameter	10 light-years
Type of Object	Supernova Remnant (SNR)
Field of View	6 x 6 arcminutes
Source Type	Extended

Table 2: Basic Radio Properties of Cassiopeia A

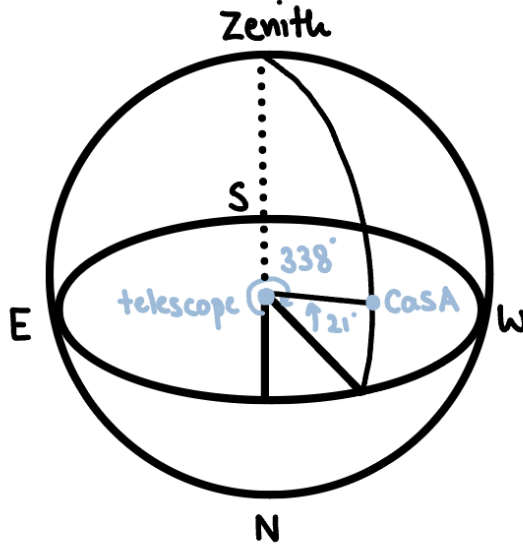| Property	Value
Telescope	Algonquin Radio Observatory (ARO)
Center (Coordinates)	RA: 03:29:11, Dec: +54:24:37
Distance	2,600 light-years
Period	0.714 s
Measure (DM)	$26.8\,\mathrm{pc/cm^3}$
Age	$2.9\,\mathrm{Myr}$
Type of Object	Isolated Pulsar
Field of View	Point Source
Emission Type	Periodic Radio Pulses

Table 3: Basic Radio Properties of Pulsar B0329+54

Figure 1: The image of ARO's pointing direction, showing an azimuth of 338° (North-Northwest) and an elevation of approximately 21°. The telescope is aimed towards Cassiopeia A in the sky as viewed on a spherical coordinate system, with the zenith directly overhead

3   Data Reduction

The data reduction process for this lab was crucial in transforming raw data from the Algonquin Radio Observatory (ARO) into a form suitable for analysis. The raw data also had several challenges due to the large observational datasets, such as noise, systematic artifacts, and the need for calibration. The reduction process started with an inspection of the metadata and headers in the binary files for both Cassiopeia A and the pulsar B0329+54. Sanity checks were performed to ensure the data was consistent with the telescope's operating parameters such as checking the frequency range (400–800 MHz) and the pointing coordinates (azimuth: 337.75°, elevation: 20.73°). Data anomalies, including missing slices or physically implausible values, were identified and excluded.

The calibration dataset from Cassiopeia A served as a benchmark for characterising the telescope's performance. Using a frequency sub-band, the telescope's beam profile was constructed by plotting power as a function of source offset. The elevation offsets were calculated as the difference between the telescope's observed elevation and the expected elevation of Cassiopeia A derived using the telescope's geographic location, observation time, as well as Cassiopeia A's equatorial coordinates. Normalized power was computed by averaging the observed power across all frequencies and scaling it to a range between 0 and 1. The Gaussian function was fitted using `scipy.optimize.curve_fit`. The Full-Width Half-Maximum (FWHM) which is a measure of the telescope's resolution, was derived from the Gaussian standard deviation ($FWHM = 2.355 \times \sigma$). The plot measured beamwidths and theoretical diffraction-limited values revealed inefficiencies likely caused by spillover, suboptimal feed illumination, or deviations in the dish's surface accuracy. The diffraction limit was calculated using the formula:

$$\text{FWHM} = 1.028 \cdot \frac{\lambda}{D},$$

where λ is the wavelength of the observed signal and D is the telescope's aperture diameter (46 meters).

The data for this plot was processed using Python code and the normalized power profiles for each frequency channel were obtained by subtracting the minimum power and scaling the data to a range between 0 and 1. A Gaussian function was fitted using Gaussian fit parameters to calculate FWHM ($2.355 \cdot \sigma$), and uncertainties were propagated from the covariance matrix output by curve fitting process ($2.355 \cdot \sqrt{\text{var}(\sigma)}$). Frequencies and beamwidths with invalid or noisy data were then filtered out to ensure the reliability of the analysis. The aperture efficiency was calculated using the formula:

$$\eta = \frac{\lambda^2}{\Omega \cdot A_g},$$

where $A_g = \pi \cdot (D/2)^2$ is the geometric area of the telescope, and $\Omega = 1.133 \cdot \text{FWHM}^2$ is the beam solid angle in steradians. Errors in aperture efficiency were propagated using:

$$\text{Error}(\eta) = \eta \cdot \frac{\text{Error}(\Omega)}{\Omega},$$

where $\text{Error}(\Omega)$ was derived from the uncertainties in FWHM. Aperture efficiency generally decreases with increasing frequency. For the pulsar B0329+54 dataset, the complexity of the time series data required additional processing. Initially, the data was visualized using waterfall plots, which revealed the dispersed nature of the pulsar signal. The raw waterfall plot of the Pulsar is foundational for subsequent data reduction steps such as de-dispersion, which aligns the signal at all frequencies by calculating the delay:

$$t_{\text{delay}} = \frac{4.15 \times 10^3 \cdot \text{DM}}{\nu_1^2 - \nu_2^2} \text{ ms},$$

where ν_1 and ν_2 represent the upper and lower bounds of the frequency band. Mitigating RFI is equally important, as residual interference can bias the pulsar analysis and reduce the accuracy of derived parameters. The frequency-dependent time delay, caused by the interstellar medium (ISM), was calculated using the known dispersion measure (DM) of B0329+54. Each frequency sub-band was time-shifted to correct for dispersion, aligning the pulsar signal across the band. The correction significantly enhanced the visibility of the pulses and reduced the noise. Following this, the data was folded over the pulsar's known period to average multiple pulses into a single phase profile. This step improved the signal to noise ratio and revealed the pulse structure of B0329+54 allowing for a more detailed analysis of its profile and variability.
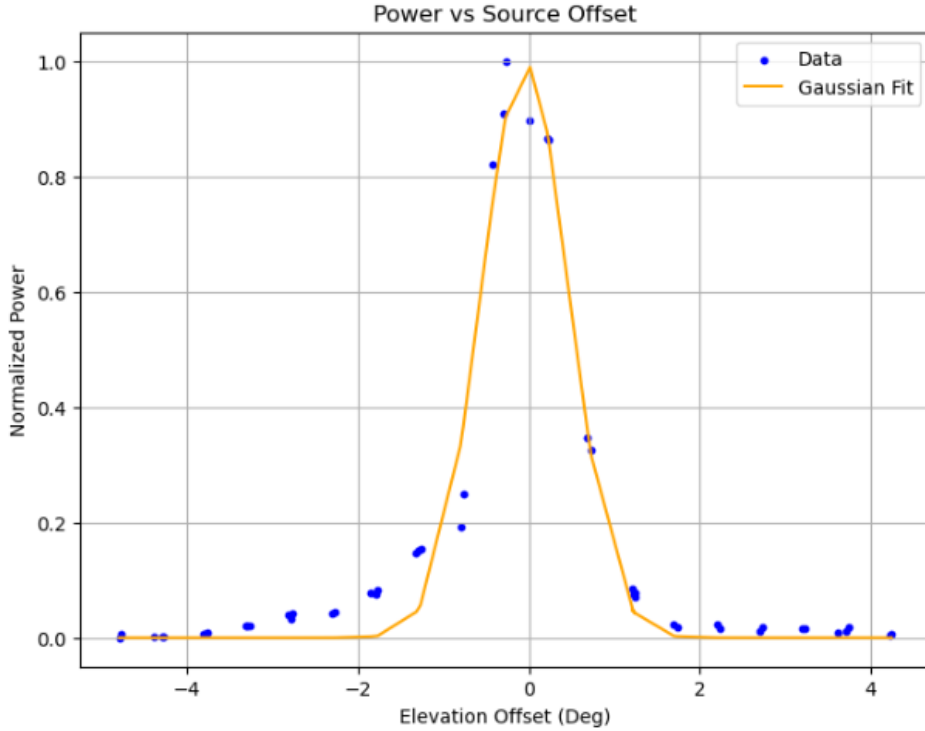
4 Data Analysis

Figure 2: This plot shows the normalized power as a function of elevation offset in degrees from the source, which illustrates the telescope's beam profile. The blue points represent the observed data whereas the orange line is a Gaussian fit that is used to model the beam's Full Width at Half Maximum (FWHM). The peak at 0° indicates the beam center, with power decreasing relatively symmetrically as the offset increases. The close alignment between the data and the fit is indicative of the telescope's well-calibrated response
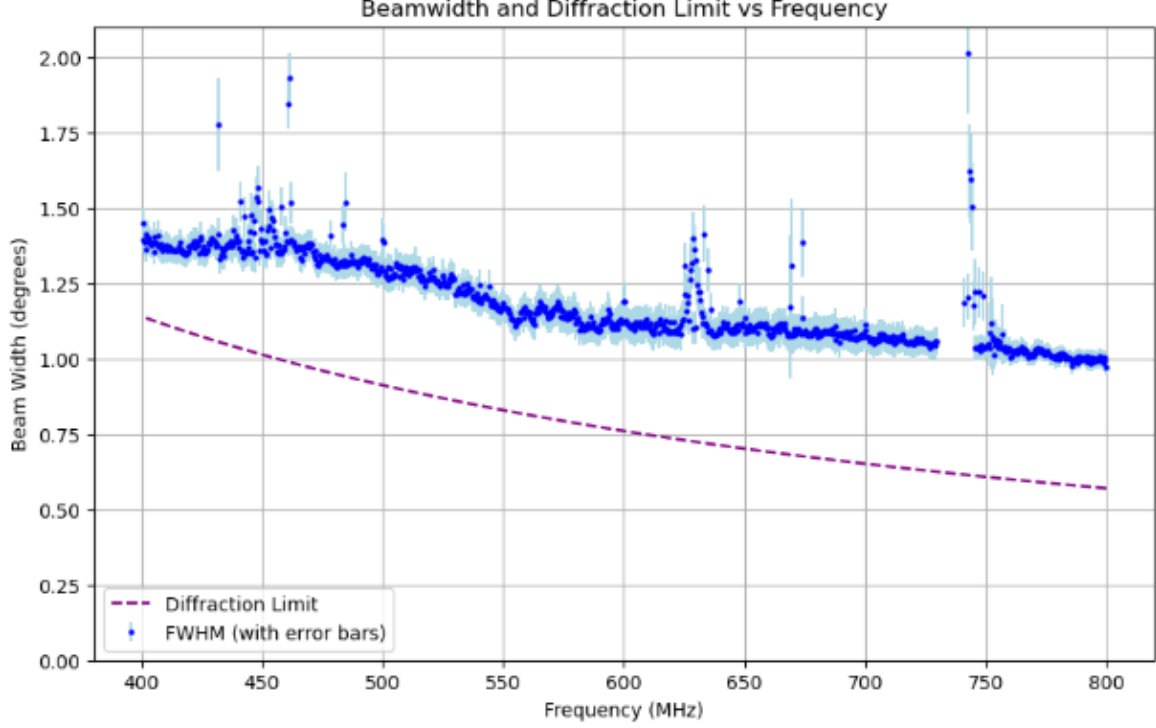
Figure 3: This plot compares the measured beamwidth (Full Width at Half Maximum, FWHM) of the telescope with its theoretical diffraction limit across frequncies of 400–800 MHz. The blue markers represent the FWHM values, with error bars indicating measurement uncertainties. The dashed purple line shows the theoretical diffraction limit, calculated using FWHM $= 1.028 \cdot \lambda/D$, where λ is the wavelength and D is the aperture diameter of the telescope. The measured FWHM closely follows the diffraction limit at higher frequencies but shows deviations at lower frequencies likely due to atmospheric effects or instrumental inefficiencies. The error bars highlight regions with increased variability showing uncertainty in the beam profile.

Figure 2 depicts normalized power as a function of elevation offset from the source Cassiopeia A. The data points, shown in blue, represent observed measurements, while the orange line represents a Gaussian fit modelling the telescope's beam profile. The Gaussian curve closely aligns with the data and indicates that the telescope's beam is symmetric and well-calibrated. The peak at 0° elevation offset confirms that the beam is centered on the source when properly aligned, with the power dropping off symmetrically as the offset increases. The narrow FWHM observed in the fit suggests that the telescope is well-focused. However, some deviations between the data points and the Gaussian fit are evident, particularly at larger offsets, which could have resulted from noise, hardware imperfections, or atmospheric effects.

This plot effectively validates the Gaussian model for characterizing the telescope's beam profile and quantifies its performance. The close alignment between the fit and the data confirms that the beam's power distribution follows theoretical expectations, while the FWHM provides a meaningful measure of the telescope's angular resolution. The results also emphasize the importance of addressing minor deviations, which could point to potential improvements in hardware or observation conditions.

Figure 3 compares the measured FWHM of the telescope's beam with the theoretical diffraction limit over a frequency range of 400–800 MHz. The blue markers represent the measured FWHM values, with error bars indicating uncertainties with a dashed purple line showing the diffraction limit. The measured FWHM values closely follow the theoretical diffraction limit at higher frequencies, indicating that the telescope operates near its optimal resolution in this range. However, at lower frequencies, the FWHM seems to deviate from the diffraction limit, likely due to instrumental limitations such as surface accuracy, spillover, or atmospheric turbulence. Furthermore, the spikes in the FWHM, especially around 650 MHz and 750 MHz, suggest potential calibration anomalies or local interference. The error bars provide insight into the measurement uncertainties, with larger error bars in regions of higher variability or lower signal-to-noise ratio such as 420-500 MHz and 620-760 MHz. However, the Gaussian curves used to derive the FWHM reinforce the reliability of the results as the data closely aligns with theoretical
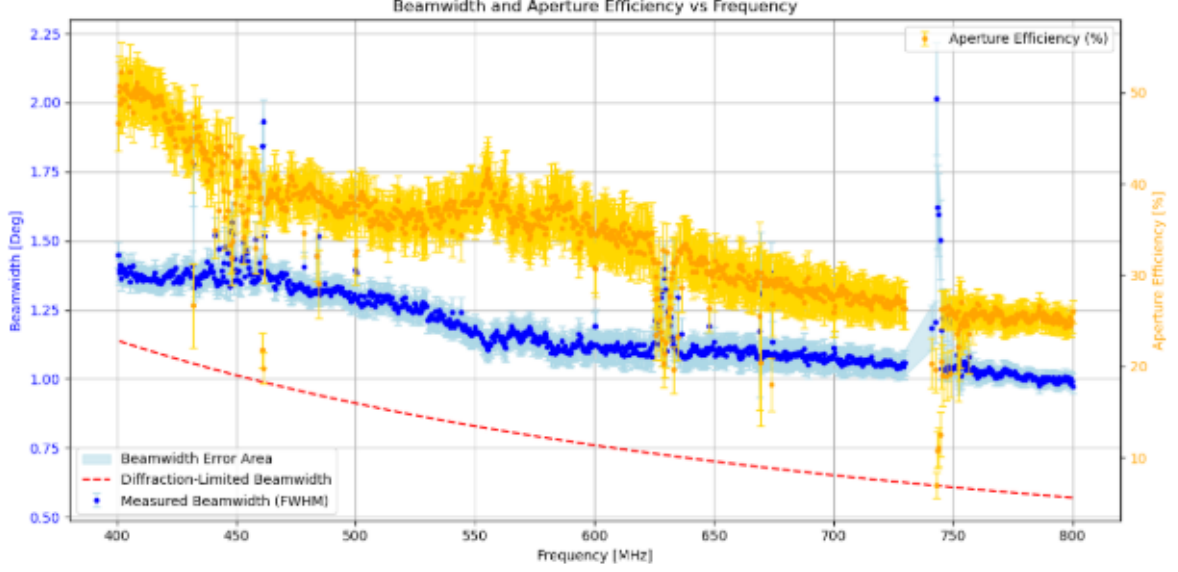
Figure 4: This plot compares the measured beamwidth (blue markers) and aperture efficiency (yellow markers) of the telescope as functions of frequency 400–800 MHz. The blue shaded area represents the beamwidth error, while the dashed red line depicts the theoretical diffraction-limited beamwidth, calculated using FWHM $= 1.028 \cdot \lambda/D$. Aperture efficiency, expressed as a percentage, is plotted on the secondary y-axis on the right and reflects the telescope's effectiveness in converting collected power into usable signal. The measured FWHM values align closely with the diffraction limit at higher frequencies but deviate at lower frequencies, indicating instrumental or atmospheric effects. Aperture efficiency shows a general decreasing trend with the frequency, consistent with expected performance variations. Error bars on both datasets indicate measurement uncertainties.

expectations in most regions.

Figure 4 displays the telescope's performance by presenting the measured beamwidth (FWHM) and aperture efficiency as functions of frequency between 400 and 800 MHz. The left y-axis represents the beamwidth in degrees, while the right y-axis shows aperture efficiency in percentage. Blue markers indicate the measured FWHM values and light blue error bars and shaded areas represent uncertainties. The dashed red line represents the theoretical diffraction limit.

The measured beamwidth closely follows the theoretical diffraction limit at higher frequencies, demonstrating the telescope's capability to operate near its optimal resolution. However, deviations are then observed at lower frequencies where the measured FWHM exceeds the diffraction limit. These discrepancies are likely due to instrument limitations which could include surface imperfections, suboptimal feed illumination, or atmospheric effects that are more pronounced at longer wavelengths.

The plot in Figure 4 shows that the alignment between the measured and theoretical beamwidth at higher frequencies validates the telescope's performance, while deviations and uncertainties at lower frequencies highlight areas for further investigation such as improving calibration or addressing environmental factors. The aperture efficiency trends provide insights into the telescope's frequency dependent performance by emphasising the importance of good calibration and continuous monitoring to ensure high quality observations.
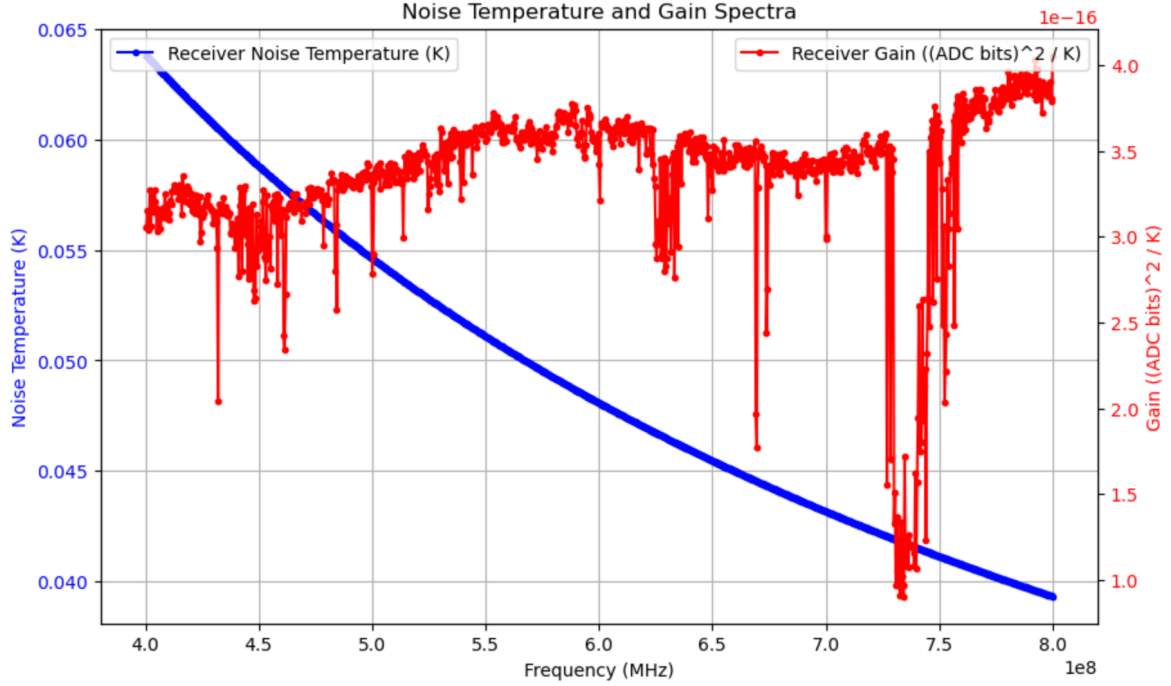
Figure 5: This plot displays the receiver noise temperature as a blue curve, left y-axis and receiver gain as a red curve, right y-axis as functions of frequency (MHz). The noise temperature, measured in Kelvin (K), decreases smoothly with increasing frequency, reflecting the receiver's intrinsic noise behaviour. The receiver gain is expressed in $(\text{ADC bits})^2/\text{K}$) shows significant variability across 400-800 MHz, with notable dips and spikes caused by systematic effects or RFI. The dual y-axes provide a clear comparison between the two parameters

Figure 5 displays the receiver noise temperature and gain as functions of frequency. The blue curve represents the receiver noise temperature, which decreases with increasing frequency as expected from the inherent noise properties of the system. The red curve shows the receiver gain with significant variability, including frequent dips and spikes across the frequencies. These fluctuations in gain are likely caused by systematic effects such as imperfections in the receiver calibration, environmental interference or RFI. From the analysis, several important parameters were derived. The flux density near 700 MHz was measured to be $1747.63\,\text{Jy} = 1.75 \times 10^{-23}\,\text{W/m}^2/\text{Hz}$ and the effective aperture of the telescope was calculated as $1080.24\,\text{m}^2$. Additionally, the estimated source temperature for Cassiopeia A in this sub-band was determined to be $684.0\,\text{K}$. The overall shape of the noise temperature curve is smooth and monotonic, which indicates a predictable decrease in thermal noise with increasing frequency. This behaviour is consistent with theoretical expectations. In contrast, the gain spectrum demonstrates substantial irregularities, including abrupt dips at specific frequencies, which may correspond to frequency-dependent losses in the system or interference from external sources. The spikes in the gain spectrum could be attributed to RFI which is a known challenge in radio astronomy, particularly in heavily used frequency bands. Certain features in the data suggest potential calibration, hardware, or analytical issues. The frequent and sharp variations in gain could indicate instabilities in the receiver system. The seemingly low temperature can be attributed to errors in the calibration procedure or unaccounted for contributions from environmental factors.
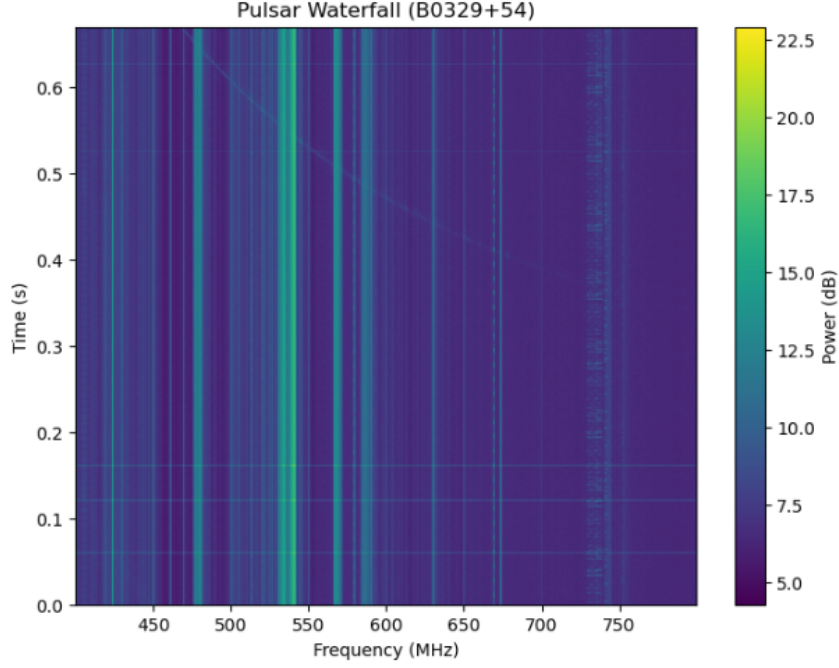
Figure 6: Waterfall plot of pulsar B0329+54 which shows power in dB as a function of frequency (MHz) and time (s). The color scale on the right indicates power levels, with brighter colors representing higher power. The diagonal streaks correspond to the dispersion of the pulsar signal caused by the interstellar medium, where higher frequencies arrive earlier than lower frequencies. Vertical lines represent frequency-dependent radio-frequency interference (RFI). This plot gives insight into the pulsar's dispersed signal and emphasises the need for dispersion correction and RFI mitigation in subsequent analysis.

The waterfall plot of pulsar B0329+54 in 6 provides a visual representation of the power (in dB) as a function of frequency (MHz) and time (s). The x-axis spans the frequency range from 400 to 800 MHz, while the y-axis covers a 0.7-second time interval. The colour scale where brighter regions indicate higher power, reveals the distribution of the pulsar signal across time and frequency.

A key feature of the plot is the diagonal streak, which corresponds to the dispersion of the pulsar signal caused by the interstellar medium (ISM). This dispersion effect occurs because lower frequency radio waves are delayed more than higher frequency waves as they travel through the ISM. The slope in the plot is consistent with the known dispersion measure (DM) of pulsar B0329+54. Correcting this effect is quite important for aligning the pulses across all frequencies and also enabling accurate phase folding and further analysis.

Vertical lines in the plot highlight the presence of radio-frequency interference (RFI), which is independent of the pulsar signal. These lines, prominent around 550 MHz and 750 MHz, likely arise from local or external sources, such as communication signals or electronic noise. The RFI contamination emphasizes the need for preprocessing techniques to isolate the pulsar's signal.

The plot also highlights variability in power levels across time and frequency. The pulsar's signal diminishes at certain frequencies, reflecting the telescope's frequency-dependent sensitivity or atmospheric effects. Additionally, fluctuations in power within the diagonal streak may indicate intrinsic pulsar emission variability or noise in the data. This variability along with the RFI contamination highlights the importance of robust preprocessing methods.

Figure 7b shows the folded power (in dB) as a function of frequency (MHz) and pulse phase (s). The periodic pulsar signal is evident in the bright regions that repeat over the pulse phase which shows the regular emission of the pulsar. The vertical lines correspond to radio-frequency interference (RFI), which affects specific frequencies and appears as consistent streaks across the phase axis. The visibility of the periodic pulses across the frequency range highlights the stability of the pulsar signal but also emphasises the importance of effective RFI mitigation for accurate analysis. The right subplot, in Figure 7 further displays the pulsar signal by renormalising the power by dividing by the median values. This process improves the contrast between the pulsar emission and the background noise and makes the periodic nature of the pulsar more distinct. The bright regions representing the pulsar emission stand out more prominently in this plot compared to the left subplot.
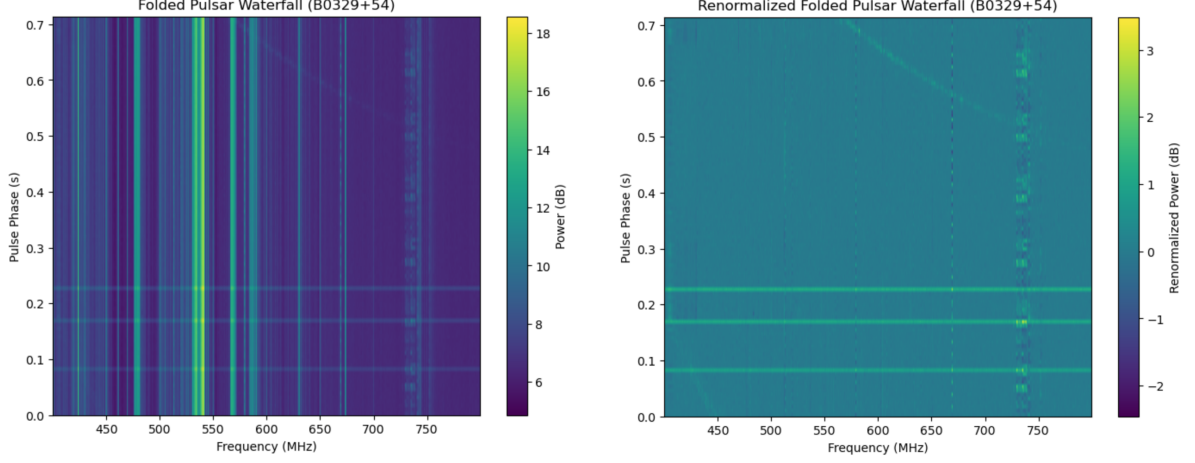
(a) Folded Pulsar Waterfall: Shows the folded power (in dB) of pulsar B0329+54 as a function of frequency (MHz) and pulse phase (s). The bright regions correspond to the periodic emission from pulsar and visible across the frequency range. Vertical lines correspond to Radio Frequency Interference (RFI) affecting specific frequencies. The folding process highlights the periodic nature of pulsar signal.

(b) Renormalized Folded Pulsar Waterfall: Shows the folded and renormalized power (in dB) of pulsar B0329+54 as a function of frequency (MHz) and pulse phase (s). The renormalisation scales the power for each frequency channel which improves the contrast between the pulsar signal and the background. The bright regions correspond to pulsar emission

Figure 7: Displays the comparison of the folded and renormalized folded waterfall plots of pulsar B0329+54. The left subplot shows the raw folded power with the periodic signal from the pulsar. The right subplot demonstrates the renormalised folded power, improving the visibility of the pulsar signal across the frequency band.
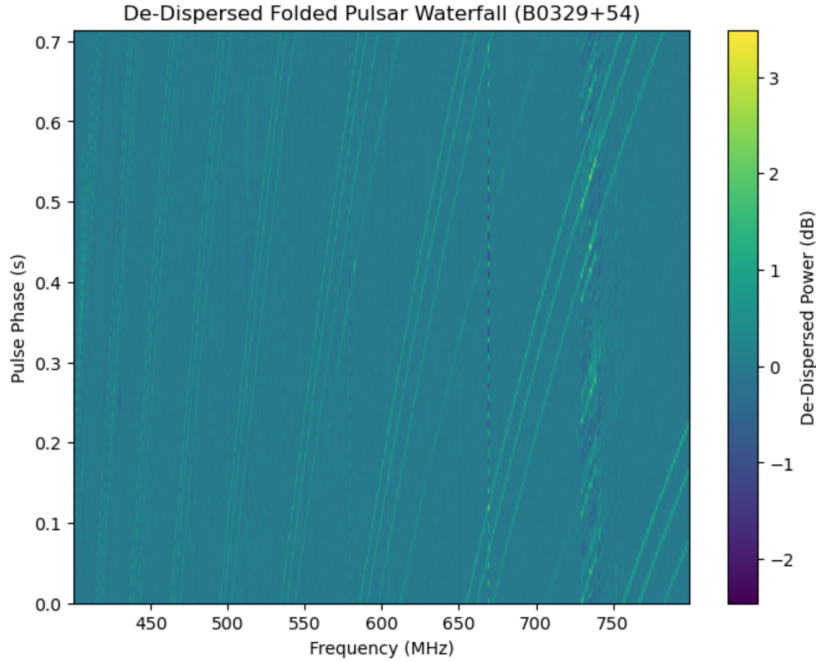

Figure 8: Plot of De-Dispersed Folded Pulsar Waterfall Plot for B0329+54. It illustrates the power (in dB) as a function of pulse phase (s) and frequency (MHz) after de-dispersion. The de-dispersion process corrects for frequency dependent delays caused by the ISM, aligning the pulse signals vertically across all frequencies. Bright vertical regions correspond to the periodic pulses of the pulsar, with clear alignment demonstrating the removal of dispersive effects.

The De-Dispersed Folded Pulsar Waterfall Plot for pulsar B0329+54 demonstrates the removal of frequency dependent dispersive delays caused by the ISM. These dispersive delays are characterised by pulse arrival times lagging at lower frequencies due to the ISM are corrected using a Dispersion Measure

(DM) of 26.8 pc/cm^3. The de-dispersion process realigned the pulse signal across all frequencies which resulted in a vertically aligned structure that reflects consistent pulse phases across the frequency band.

Before de-dispersion, the folded waterfall plot exhibited dispersive delays that appeared as a diagonal streak, where pulses arrived earlier at higher frequencies and progressively later at lower frequencies. This dispersion obscured the pulsar's periodic signal. After de-dispersion, the pulses became vertically aligned across all the frequencies which clearly resolved the periodic emission at the expected pulse phases. The plot prominently displays power peaks at specific pulse phases, confirming the removal of ISM induced delays.
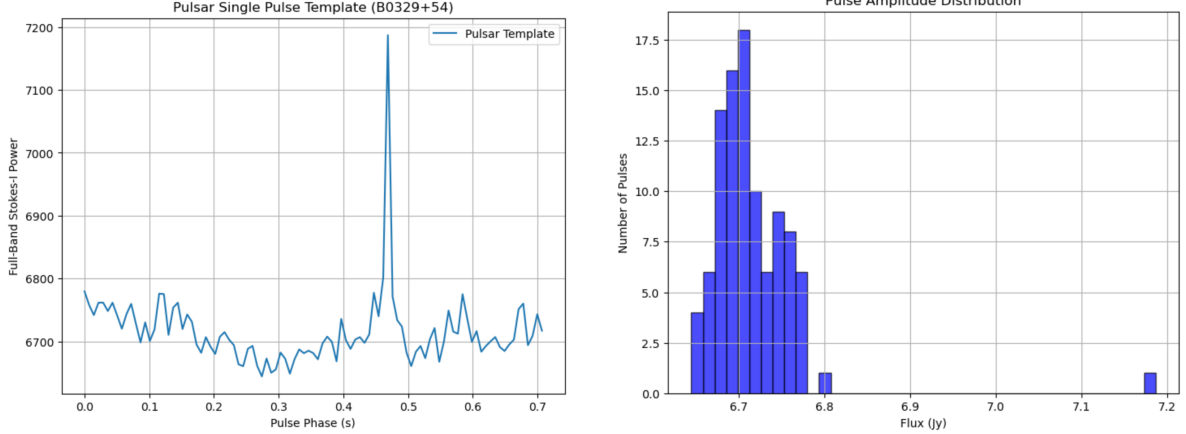
(a) Single Pulse Template: This plot shows the full-band Stokes-I power as function of pulse phase for pulsar B0329+54. The sharp peak at around 0.45 s highlights the typical emission profile of a single pulse with the surrounding regions representing noise and baseline levels. Derived by de-dispersing and summing across the frequency band.

(b) Pulse Amplitude Distribution: This histogram represents the flux distribution of individual pulsar pulses for B0329+54, measured in Janskys (Jy). The majority of the pulses have flux values between 6.7 Jy and 6.8 Jy, with a small number of higher-intensity outliers. The distribution reflects the variability in pulsar pulse amplitudes.

Figure 9: Analysis of pulsar B0329+54's single pulse properties. (a) shows the typical pulse template obtained by folding, de-dispersing, and summing the frequency band. (b) presents the flux amplitude distribution, showing the variation in intensity across individual pulses.

Figure 9 analyses the pulsar B0329+54's single pulse properties by showing both the typical pulse profile and the variability in pulse amplitudes. The single pulse profile plot in Figure 9a illustrates the full-band Stokes-I power as a function of pulse phase. This is derived by folding the data at the pulsar's period, de-dispersing it and then summing across all frequency channels. The sharp peak observed near a phase of 0.45 s represents the intrinsic emission from the pulsar while the flatter baseline indicates noise and background levels. If a full band profile is calculated without de-dispersion, the dispersive effects of the ISM cause the pulses from different frequency channels to arrive at different times and smear the signal across multiple pulse phases. This significantly diminishes the sharpness of the pulse and also reduces the peak intensity.

The pulse amplitude distribution plot in Figure 9b highlights the variability in individual pulse intensities. The histogram shows that the majority of pulses have flux values between 6.7 Jy and 6.8 Jy, with a small number of high-intensity outliers. This variability is a common feature of pulsar emission often attributed to intrinsic fluctuations in the pulsar's emission mechanism or propagation effects in the ISM. The presence of outliers can indicate occasional strong pulses or errors caused by RFI.

Figure 10 shows the unfolded full-band Stokes-I power as a function of time for pulsar B0329+54. This provides a direct view of the pulsar's activity over the observation period and shows significant variability in the signal. The sharp peak at approximately 0.35 seconds is indicative of a pulsar pulse, while the surrounding variations correspond to background noise and also baseline fluctuations. The use of unfolded data ensures that no periodic averaging or folding is applied which allows for clear visualisation of the raw pulse signal. The periodicity observed in the data is approximately 0.7 seconds which aligns with the known pulse period of B0329+54. This confirms the accuracy of the observation and the synchronization of the data collection with the pulsar's intrinsic period. The periodicity is critical for identifying pulsar pulses, and any deviation from the expected value could suggest either a mismatch in folding parameters or potential issues in the data processing pipeline.

Figure 11 provides insights into the pulse detection and timing properties of pulsar B0329+54. The
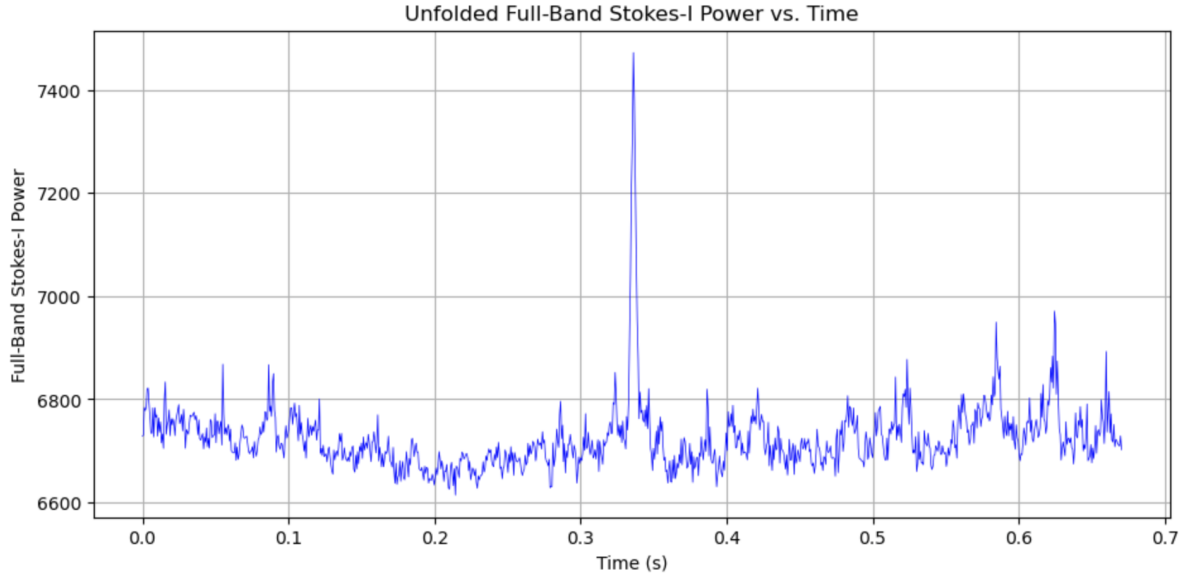
Figure 10: Unfolded Full-Band Stokes-I Power vs. Time for Pulsar B0329+54. This plot represents the time domain variation of the full-band Stokes-I power without folding or averaging. The sharp peak near 0.35 seconds corresponds to a pulsar pulse while the surrounding variations indicate noise and baseline fluctuations. The absence of folding emphasizes the variability in pulse amplitudes and intervals. This provides a direct view of pulsar activity over the observation period.
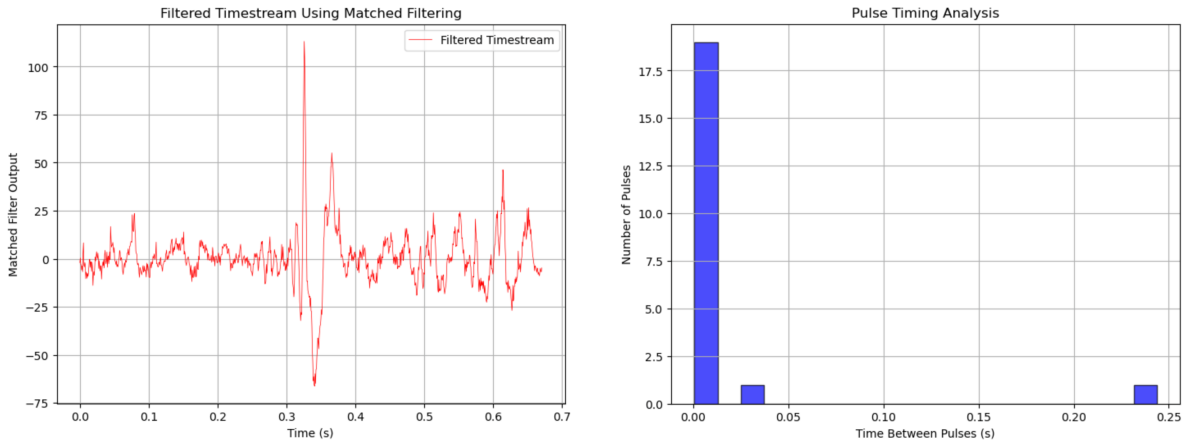
(a) Filtered Timestream Using Matched Filtering: Shows the matched filter output for the pulsar B0329+54 as a function of time. The matched filter amplifies the periodic signal, highlighting individual pulses as sharp peaks, with the most prominent pulse near 0.35 seconds. This technique optimises sensitivity to pulsar signals.

(b) Pulse Timing Analysis: This histogram represents the distribution of time intervals between consecutive pulses for B0329+54. Most of the pulses are detected at consistent intervals, corresponding to the pulsar's intrinsic period. The small number of outliers likely results from noise or inaccuracies in the timing resolution.

Figure 11: Analysis of pulsar B0329+54's pulse timing using matched filtering. (a) illustrates the matched filter's effectiveness in enhancing the pulsar's periodic signal and (b) evaluates the regularity of pulse timing showing that most pulses occur at consistent intervals.

filtered time stream plot demonstrates the application of a matched filter to the data, while the pulse timing analysis histogram shows the consistency of the intervals between detected pulses.

The plot in Figure 11a shows the matched filter output which highlights the periodic pulsar signals as sharp peaks against the noise. The use of template convolution, a simplified version of matched filtering, is highly effective in isolating the pulses as it maximizes the sensitivity to signals that match the template's shape. This works by convolving the observed time stream with the average pulse profile template, which enhances the regions in the data that resemble the template while suppressing random noise. Matched filtering detects signals of interest here such as pulsar pulses, in noisy environments.

11

The histogram of pulse timing analysis reveals that the pulses occur at consistent intervals, confirming the intrinsic period of the pulsar. In this case, the pulses consistently align with the expected period of 0.714 seconds, indicating that the folding and timing calculations were performed correctly. There is no evidence of the pulse "moving around" within its period which suggests the data processing, including de-dispersion and template matching, was properly executed. The small number of outliers in the histogram are likely results from noise, low signal to noise ratio events, or occasional interference.

5 Discussion & Conclusion

The results of this investigation into the performance of the Algonquin Radio Observatory's 46m telescope and also the analysis of pulsar B0329+54 have provided valuable insights into both instrumental characteristics and astrophysical phenomena. Through calibration and data analysis, this study has demonstrated the telescope's capabilities while also identifying areas for improvement and further exploration.

The beamwidth analysis, summarized in Figure 4, reveals that the measured Full Width at Half Maximum (FWHM) closely follows the theoretical diffraction limit at higher frequencies but deviates at lower frequencies. These deviations are likely due to instrumental inefficiencies such as the suboptimal feed illumination, surface inaccuracies, or atmospheric effects which are more pronounced at longer wavelengths. The aperture efficiency shown alongside the beamwidth demonstrates a gradual decline with increase in frequency, consistent with expected performance trends. However, occasional spikes and dips in efficiency, such as those observed around 700 MHz, highlight potential issues with calibration or localised RFI. The effective aperture of the telescope was found to be $1080.24 \, \text{m}^2$ which provides a direct measure of the telescope's collecting area.

The receiver noise temperature and gain spectra, depicted in Figure 5 further illustrate the telescope's performance. The noise temperature decreases monotonically with frequency and is consistent with theoretical expectations and demonstrates the receiver's predictable thermal noise behaviour. The gain spectrum however, exhibits significant variability, including abrupt dips and spikes which are indicative of systematic issues or environmental interference. These irregularities emphasize the need for further investigation into receiver stability and improved RFI mitigation strategies. Additionally, the derived flux density was determined to be $1.75 \times 10^{-23} \, \text{W/m}^2/\text{Hz}$ and the estimated source temperature was $684.0 \, \text{K}$ for Cassiopeia A.

The pulsar analysis focused on B0329+54 demonstrates the importance of data reduction and processing techniques. The waterfall plots, as shown in Figures ?? and 7, effectively highlight the challenges posed by dispersion and RFI. The diagonal streaks in the raw waterfall plot reveal the dispersion delay which is caused by the interstellar medium (ISM), while vertical lines expose frequency-dependent RFI contamination. The process of de-dispersion, as illustrated in Figure 8 managed to correct these delays, aligning the pulsar signals across all frequencies. This not only enhanced the visibility of the periodic emission but also allowed accurate folding of the pulsar data.

Matched filtering, shown in Figure 11a, proved to be a critical technique for amplifying the pulsar's periodic signal against the noise. The sharp peaks in the filtered time stream reflect the effectiveness of this approach in isolating individual pulses. The pulse timing analysis further validated the pulsar's intrinsic period of 0.714 seconds, with minimal deviations from expected intervals. However, the presence of outliers in the timing distribution highlights the need for RFI suppression and noise reduction.

Despite the overall success of this analysis, certain limitations were identified. The frequent variability in gain and the occasional deviations in measured beamwidth suggest that enhanced calibration techniques and improved receiver stability is required. Additionally, the significant RFI contamination observed in the pulsar data highlights the importance of implementing more thorough interference mitigation strategies in future observations. Future work could explore the application of adaptive RFI filtering techniques and advanced beam shaping algorithms to further improve telescope performance. The integration of real time data processing pipelines for dispersion correction and pulse detection could also enhance the efficiency of these pulsar observations. Moreover, extending this analysis to other pulsars and celestial sources would provide a broader validation of the methods and insights that were presented in this study.

In conclusion, this investigation has demonstrated the capabilities of the Algonquin 46m telescope and provided a detailed analysis of pulsar B0329+54. The derived results, including beamwidth, noise temperature, aperture efficiency, and pulsar parameters, align with theoretical expectations and established literature values. These findings contribute to our understanding of radio telescope performance and pulsar behavior, while also identifying avenues for future improvements.

6 Bibliography

ASTROLab du parc national du Mont-Mégantic (no date) *The Algonquin Radio Observatory: Observatories, Canada under the stars.* Available at: https://astro-canada.ca/l_observatoire_algonquin_de_radioastronomie-the_algonquin_radio_observatory-eng (Accessed: 03 February 2025).

Cassiopeia A (2020) *National Radio Astronomy Observatory.* Available at: https://public.nrao.edu/gallery/cassiopeia-a/ (Accessed: 03 February 2025).

Cordes, J.M. & Lazio, T.J.W., 2002. *NE2001.I. A New Model for the Galactic Distribution of Free Electrons and Its Fluctuations. Astronomy & Astrophysics*, 376, pp.763–781. Available at: https://www.aanda.org/articles/aa/pdf/2001/43/aa1712.pdf https://www.aanda.org/articles/aa/pdf/2001/43/aa1712.pdf (Accessed 21 January 2025).

Department of Astronomy and Astrophysics, *Thermal Radiation & the Statistics of Noise*: Lab Manual for AST325/326 (Fall 2024), University of Toronto, October 2024.

Yao, J.M., Manchester, R.N. & Wang, N., 2022. *A New Electron-density Model for Estimating Galactic Distances. Astronomy & Astrophysics*, 657, A15. Available at: https://www.aanda.org/articles/aa/abs/2022/01/aa42099-21/aa42099-21.html https://www.aanda.org/articles/aa/abs/2022/01/aa42099-21/aa42099-21.html (Accessed 1 February 2025).

Appendix:

A Derivations

A.1. Computing the Diffraction-Limited Beamwidth

The theoretical diffraction-limited beamwidth for a circular aperture telescope is given using:

$$\text{FWHM} = 1.028 \cdot \frac{\lambda}{D},$$

where λ is the wavelength of the observed signal and D is the diameter of the telescope aperture. This formula is derived from the diffraction pattern produced by a circular aperture, which results in an Airy disk. The Full Width at Half Maximum (FWHM) corresponds to the angular separation between points in the diffraction pattern where the intensity falls to half the maximum value. The proportionality constant 1.028 comes from the first zero of the Airy disk pattern.

A.2. Uncertainty in Beamwidth (FWHM)

The Full Width at Half Maximum (FWHM) is calculated from the Gaussian fit using the relation:

$$\text{FWHM} = 2.355 \cdot \sigma,$$

where σ is the standard deviation of the Gaussian fit. The uncertainty in FWHM is propagated from the uncertainty in σ, which is given by the variance obtained from the covariance matrix during the fitting process:

$$\text{Error in FWHM} = 2.355 \cdot \sqrt{\text{var}(\sigma)}.$$

This error provides a quantitative measurement of the confidence for the beamwidth values.

A.3. Uncertainty in Aperture Efficiency

The aperture efficiency η is defined as:

$$\eta = \frac{\lambda^2}{\Omega \cdot A_g},$$

where λ is the wavelength, $\Omega = 1.133 \cdot \mathrm{FWHM}^2$ is the beam solid angle, and $A_g = \pi \cdot \left(\frac{D}{2}\right)^2$ is the geometric area of the telescope. The uncertainty in η is derived by propagating the uncertainties in Ω and A_g using the relation:

$$\mathrm{Error}(\eta) = \eta \cdot \frac{\mathrm{Error}(\Omega)}{\Omega}.$$

The uncertainty in Ω is calculated as:

$$\mathrm{Error}(\Omega) = 2 \cdot 1.133 \cdot \mathrm{FWHM} \cdot \mathrm{Error}(\mathrm{FWHM}),$$

where $\mathrm{Error}(\mathrm{FWHM})$ is obtained from the Gaussian fit.

A.4. Uncertainty in Dispersion Measure (DM)

The delay caused by the interstellar medium (ISM) is due to the dispersion measure (DM) is given by the following:

$$t_{\mathrm{delay}} = \frac{4.15 \times 10^3 \cdot \mathrm{DM}}{\nu_1^2 - \nu_2^2} \, \mathrm{ms},$$

where ν_1 and ν_2 are the upper and lower frequency bounds in MHz and DM is the dispersion measure in pc/cm^3. The uncertainty in t_{delay} is derived by propagating the uncertainties in ν_1, ν_2 and DM of:

$$\mathrm{Error}(t_{\mathrm{delay}}) = t_{\mathrm{delay}} \cdot \sqrt{\left(\frac{\mathrm{Error}(\mathrm{DM})}{\mathrm{DM}}\right)^2 + \left(\frac{\mathrm{Error}(\nu_1)}{\nu_1}\right)^2 + \left(\frac{\mathrm{Error}(\nu_2)}{\nu_2}\right)^2}.$$

This provides an assessment of the impact of measurement errors on the given time delay.

B   Code

B.0.1   Code to Plot Power vs Source Offset

```python
# import all the required libraries
import numpy as np
import matplotlib.pyplot as plt
from scipy.optimize import curve_fit

# define the Gaussian function thats used for curve fitting
def gaussian(x, amp, mu, sigma):
    return amp * np.exp(-0.5 * ((x-mu) / sigma)** 2)

# now computing source offset
offsets = casa_el - el
# averaging power across all frequencies for normalisation
power_sum = nd.mean(axis=1)

# normalising power
power_sum -= np.min(power_sum)
power_sum /= np.max(power_sum)

# fitting thw Gaussian to data
popt, _ = curve_fit(gaussian, offsets, power_sum, p0=[1, 0, 1])
amp, mu, sigma = popt
# computing # Full-Width Half-Maximum
fwhm = 2.355*sigma

# plotting Power vs Offset
plt.figure(figsize=(8, 6))
plt.scatter(offsets, power_sum, s=10, label="Data", color="blue")
plt.title("Power vs Source Offset")
plt.plot(offsets, gaussian(offsets, *popt), label=f"Gaussian Fit", color="orange")
plt.xlabel("Elevation Offset (Deg)")
plt.ylabel("Normalized Power")

plt.legend()
plt.grid()
plt.show()
```

Listing 1: Python code for plotting the power against source offset

B.0.2 Code to Plot Beamwidth and Aperture Efficiency vs Frequency

```python
# import the required libraries
import numpy as np
import matplotlib.pyplot as plt

# define the constants needed
c = 3e8  # speed of light in m/s
diam = 46  # Telescope diameter in meters
area = np.pi * (diam / 2) ** 2  # Geometric area in m^2

# creating empty lists for theoretical diffraction-limited beamwidth and aperture
    efficiency
diff_limit_deg = []
aper_eff = []
aper_eff_errors = []

# calculate these values with for loops
for freq_mhz, fwhm_deg, fwhm_err_deg in zip(filtered_frequencies, filtered_beamwidths,
    filtered_errors):
    freq_hz = freq_mhz*1e6
    # getting wavelenght in meters
    wavelength = c/freq_hz

    # diffraction limit
    theta_radians = 1.22 * (wavelength/diam)
    theta_degrees = np.rad2deg(theta_radians)
    diff_limit_deg.append(theta_degrees)
    # aperture efficiency
    fwhm_radians = np.deg2rad(fwhm_deg)  # FWHM to radians
    fwhm_err_radians = np.deg2rad(fwhm_err_deg)  # FWHM errors to radians
    omega = 1.133 * (fwhm_radians** 2)
    omega_err = 2*1.133 * fwhm_radians * fwhm_err_radians
    ae = (wavelength ** 2) / (omega*area)  # aperture efficiency formula
    ae_err = ae * (omega_err / omega)
    # to %
    aper_eff.append(ae*100)
    aper_eff_errors.append(ae_err * 100)

# converting the numpy arrays
diff_limit_deg = np.array(diff_limit_deg)
aper_eff = np.array(aper_eff)
aper_eff_errors = np.array(aper_eff_errors)

# plotting Beamwidth and Aperture Efficiency vs Frequency on same axis
fig, ax1 = plt.subplots(figsize=(12, 6))

# plotting beamwidth on the left y-axis
ax1.errorbar(filtered_frequencies, filtered_beamwidths, yerr=filtered_errors, fmt=".",
    color="blue", ecolor="lightblue",
            elinewidth=1, capsize=3, label="Measured Beamwidth (FWHM)")
ax1.fill_between(filtered_frequencies, filtered_beamwidths - filtered_errors,
    filtered_beamwidths + filtered_errors,
                color="lightblue", alpha=0.5, label="Beamwidth Error Area")
ax1.plot(filtered_frequencies, diff_limit_deg, label="Diffraction-Limited Beamwidth",
    color="red", linestyle="--")
ax1.set_xlabel("Frequency [MHz]")
ax1.set_ylabel("Beamwidth [Deg]", color="blue")
ax1.tick_params(axis="y", labelcolor="blue")
ax1.legend(loc="lower left")
ax1.grid()

# plotting aperture efficiency on the right y-axis and error bars
ax2 = ax1.twinx()
ax2.errorbar(filtered_frequencies, aper_eff, yerr=aper_eff_errors, fmt=".", color="
    orange", ecolor="gold",
            elinewidth=1, capsize=3, label="Aperture Efficiency (%)")
ax2.set_ylabel("Aperture Efficiency [%]", color="orange")
ax2.tick_params(axis="y", labelcolor="orange")
ax2.legend(loc="upper right")
plt.title("Beamwidth and Aperture Efficiency vs Frequency")
plt.tight_layout()
```

```
66  plt.show()
```
Listing 2: Python code for plotting Beamwidth and Aperture Efficiency vs Frequency with uncertainties and diffraction limited beamwidth

B.0.3 Code to determine flux density, effective aperture and estimated source temperature

```
1
2  # section 4.2
3
4  # import the libraries
5  import numpy as np
6
7  # define the constants
8  c = 3.0e8        # speed of light
9  D = 46.0         # ARO dish diameter in m
10 k = 1.38e-23     # Boltzmann constant (J/K)
11 S1GHz_1977 = 2723.0  # flux density in Jy (1 Jy = 1e-26 W/m^2/Hz)
12 dim = 0.5 # assuming a 50% dimming since 1977
13 alpha = 0.7      # Spectral index
14
15 # find what the star has dimmed to now
16 S1GHz_current = S1GHz_1977 * dim  # Jy
17
18 # choose the representative band
19 freq_center = 700e6  # Hz
20 # find flux at the sub-band center using the standard power law S        ^(-  )
21 S_subband = S1GHz_current * (freq_center/1.0e9)**(-alpha)  # in Jy
22 # Jy to W/m^2/Hz (1 Jy = 1e-26 W/m^2/Hz)
23 S_subband_W = S_subband * 1e-26
24 print(f"Flux density near 700 MHz: {S_subband:.2f} Jy = {S_subband_W:.2e} W/m^2/Hz")
25
26 # estimating the effective aperture
27 eta = 0.65
28 A_eff = eta * np.pi * (D / 2.0)**2
29 print(f"Effective aperture: {A_eff:.2f} m^2")
30
31 # calculating the source temperature for a point source that (mostly) fits within the
        beam.
32 T_src = (S_subband_W * A_eff) / (2.0*k)
33 print(f"Estimated source temperature (Cassiopeia A) in this sub-band: {T_src:.1f} K")
```
Listing 3: Python code for determining flux density

B.0.4 Code to Plot Noise Temperature and Gain spectra against Frequency

```
1
2  # import the libraries
3  import numpy as np
4  import matplotlib.pyplot as plt
5
6  # define constants
7  delta_nu = 390e3  # bandwidth of each sub-band in Hz
8  t_sky = 10  # sky temp in Kelvin
9
10 # conversion constants
11 alpha = 0.7  # spectral index
12 jy_to_wm2hz = 1e-26
13 # current flux density at 1 GHz
14 S1GHz_current = S1GHz_1977 * dim
15
16 t_sys = []
17 t_rec = []
18 gains = []
19 # looping through each frequency sub-band
20 for i, freq_mhz in enumerate(nfl):
21     freq_hz = freq_mhz * 1e6
22     S_freq = S1GHz_current * (freq_hz / 1.0e9)**(-alpha)  # flux density at this freq
23     S_freq_w = S_freq * jy_to_wm2hz  # convert to W/m^2/Hz
24     # system temp
```

```
25    T_src = (S_freq_w * A_eff) / (2 * k)  # source temp (K)
26    T_sys_band = T_src + t_sky  # total system temp
27    t_sys.append(T_sys_band)
28    # gain
29    mean_power = np.mean(nd[:, i])  # average power
30    gain = (delta_nu * k * T_sys_band) / mean_power
31    gains.append(gain)
32    # receiver temp
33    T_rec_band = T_sys_band - t_sky
34    t_rec.append(T_rec_band)
35
36 # Convert to numpy arrays
37 frequencies = np.array(nfl)  # in MHz
38 t_rec = np.array(t_rec)
39 t_sys = np.array(t_sys)
40 gains = np.array(gains)
41
42 fig, ax1 = plt.subplots(figsize=(10, 6))
43
44 # plotting Noise Temperature
45 ax1.plot(frequencies, t_rec, '.-', label="Receiver Noise Temperature (K)", color='blue')
46 ax1.set_xlabel("Frequency (MHz)")
47 ax1.set_ylabel("Noise Temperature (K)", color='b')
48 ax1.tick_params(axis='y', labelcolor='b')
49 ax1.legend(loc="upper left")
50 plt.grid()
51 # plotting Gain
52 ax2 = ax1.twinx()
53 ax2.plot(frequencies, gains, '.-', label="Receiver Gain ((ADC bits)^2 / K)", color='red'
       )
54 ax2.set_ylabel("Gain ((ADC bits)^2 / K)", color='r')
55 ax2.tick_params(axis='y', labelcolor='r')
56 ax2.legend(loc="upper right")
57 plt.title("Noise Temperature and Gain Spectra")
58 plt.show()
```

Listing 4: Python code for plotting Noise Temperature and Gain spectra against Frequency

B.0.5   Code to plot Pulsar

```
1
2 if __name__ == "__main__":
3     # Replace this with the actual filename:
4     filename = "AST326_ARO_B0329+54.v01.dat"
5
6     time_sec, freqs, waterfall = read_pulsar_data(filename)
7     # converting intensities to dB (optional)
8     waterfall_dB = 10 * np.log10(waterfall + 1e-10)
9
10    # making a waterfall plot: time vs frequency
11    plt.figure(figsize=(8, 6))
12    plt.imshow(
13        waterfall_dB,
14        aspect='auto',
15        origin='lower',
16        extent=[freqs.min(), freqs.max(), time_sec.min(), time_sec.max()],
17        cmap='viridis'
18    )
19    plt.colorbar(label='Power (dB)')
20    plt.xlabel("Frequency (MHz)")
21    plt.ylabel("Time (s)")
22    plt.title("Pulsar Waterfall (B0329+54)")
23    plt.show()
```

Listing 5: Python code to plot Pulsar

B.0.6   Code to convolve time stream and plot histogram

```
1
2 import numpy as np
```

```python
import matplotlib.pyplot as plt
from scipy.signal import fftconvolve

def convolve(timestream, template):
    """
    Convolve the timestream with the normalized template for matched filtering.
    """
    # normalize template
    template = (template-np.mean(template)) / np.std(template)

    # using the FFT-based convolution for efficiency
    filter_time = fftconvolve(timestream, template[::-1], mode='same')
    return filter_time

if __name__ == "__main__":
    filename = "AST326_ARO_B0329+54.v01.dat"
    time_sec, freqs, waterfall = read_pulsar_data(filename)

    if time_sec is not None:
        # have pulsar properties
        pulse_period = 0.714  # in seconds
        DM = 26.8
        # de-disperse the data
        waterf_dedisp = dedisperse_data(waterfall, freqs, time_sec, DM)
        # sum across frequency to get full-band Stokes-I power
        full_band_power = np.sum(waterf_dedisp, axis=1)
        # normalize timestream
        full_band_power = (full_band_power-np.mean(full_band_power)) / np.std(
    full_band_power)
        # fold the data to get the template
        phase_bins, folded_power = fold_pulsar_data(time_sec, np.array([0]),
    full_band_power[:, np.newaxis], pulse_period)
        template = np.mean(folded_power, axis=1)
        # convolve timestream with template
        filter_time = convolve(full_band_power, template)
        # plotting
        plt.figure(figsize=(8, 6))
        plt.plot(time_sec, filter_time, color="red", linewidth=0.5, label="Filtered
    Timestream")
        plt.xlabel("Time (s)")
        plt.ylabel("Matched Filter Output")
        plt.title("Filtered Timestream Using Matched Filtering")
        plt.legend()
        plt.grid()
        plt.show()
        # analyse pulse timing
        threshold = np.mean(filter_time) + 2 * np.std(filter_time)
        pulse_indices = np.where(filter_time > threshold)[0]
        pulse_times = time_sec[pulse_indices]
        # check if pulses align with the known period
        pulse_differences = np.diff(pulse_times)
        plt.figure(figsize=(8, 6))
        plt.hist(pulse_differences, bins=20, color="blue", edgecolor="black", alpha=0.7)
        plt.xlabel("Time Between Pulses (s)")
        plt.ylabel("Number of Pulses")
        plt.title("Pulse Timing Analysis")
        plt.grid()
        plt.show()
```

Listing 6: Python code to convolve time stream and plot histogram